Supporting Information

Correlating Elastic Properties and Molecular Organization of an Ionic Organic Nanostructure

Jeremy R. Eskelsen,[a] Yun Qi,[b] Samantha Schneider-Pollack,[c] Samantha Schmitt,[d] K. W. Hipps,*[a] and Ursula Mazur*[a]

[a] *Department of Chemistry and Materials Science and Engineering Program, Washington State University, Pullman, WA, 99164-4630 United States. E-mail: umazur@wsu.edu; Fax: +509-335-886; Tel: +509-335-5822. E-mail: hipps@wsu.edu; Fax: +509-335-886; Tel: +509-335-3033*
[b] *Charles Evans & Associates, Sunnyvale, CA, 9408, United States*
[c] *Alfred University, Alfred, NY, 1480, United States*
[d] *Department of Material Science and Engineering, University of Wisconsin, Madison, WI, 5370, United States*

Synthesis of TSPP:TPyP self assemblies.

Materials and Sample Preparation. The meso-tetra(4-pyridyl)porphyrin H_2TPyP was purchased from Sigma Aldrich and used without further purification. The diacid form of the meso-tetra(4-sulfonatophenyl)porphyrin $H_4[H_4TSPP]Cl_2$ was purchased from Frontier Scientific and used without further purification. Concentrated HCl used for pH adjustment was reagent grade. 18 MΩ Millipore water was used in all the syntheses.

The nanorods of TSPP and TPyP were prepared as follows. A 500 μM TPyP stock solution at pH 2 was prepared by first dissolving the TPyP crystals in a lower pH smaller volume of water (to assure total dissolution of the TPyP solid) and then diluting the mixture to the desired final concentration. The stock solution of TSPP was also made at 500 μM concentration by dissolving in water but at a higher pH of 3.2 in order to minimize self-aggregation of the porphyrin with time. To prepare stoichiometric TSPP:TPyP solid nanostructures, a pH 2 solution was prepared by adding a calculated amount of 1M HCl (1:100 by volume where the latter is the final volume of the solution) followed by equal volumes of the porphyrin stock solutions. The mixture was then diluted to the desired final concentration with water. Samples were then shaken and allowed to age for at least three days to ensure complete precipitation. We found that TSPP and TPyP nanorods synthesized by adding equimolar concentrations of both tectons in pH 2 solutions resulted in the same ionic solid that was produced by the previously described procedure. Solutions of the TSPP and TPyP with different stoichiometric ratios namely, 3:1, 2:1, 1:1, 1:2, and 1:3 were prepared according to the procedure given above.

Solid samples of TSPP:TPyP nanorods were filtered from solution through a 0.1 μm pore size, 47 mm Teflon filter membrane from Membrane Solutions. The surface of the hydrophilic membrane was first moistened with a few drops of 100% ethanol prior to filtration of the aqueous nanorods solution. Solid nanorod samples were dried in air and stored in the dark.

Elemental analysis on several unheated nanorod samples were performed by Columbia Analytical Services in Tucson, AZ: http://www.caslab.com/Tucson-Laboratory/.

UV-Vis Spectral Acquisition: These spectra were obtained in 1 cm path length quartz cuvettes on a Perkin-Elmer 330 dual-beam spectrometer. Solutions were allowed to stand for sufficient time to allow the spectral intensities of the aggregates to become constant.

Ionic self-assembly of TSPP:TPyP studied by UV-visible spectroscopy

Fig. S1 shows the electronic spectra of TSPP, TPyP, and a 1:1 ratio of TSPP:TPyP in pH 2 aqueous solutions. The absorbance spectrum of TSPP monomer displays a Soret band at 434 nm indicating that the porphyrin exists in a diacid form where the inner nitrogen system is protonated to give a net +2 charge.[1] The sulfonate groups on the porphyrin ring are expected to remain unprotonated.[2,3,4] In pH 2 solutions the TPyP is expected to exist in its the free base form with a Soret band near 420 nm.[5] The imino nitrogens of the TPyP core have a pKa value of 1.1. The pyridyl nitrogens in TPyP are believed to be protonated near pH 2.3 based on the measured pK_a value of 5.25 for pyridine in aqueous solutions. To our knowledge, no one has ever directly measured the pKa of the pyridyl groups in the TPyP itself. However, the pyridyl groups of the tin complex of TPyP were reported to be protonated at pH 2.[6] Thus, one would expect be a significant concentration of TPyP ions with two or more protonated pyridyl groups such as $H_2[SnTPyP]^{2+}$ and $H_4[SnTPyP]^{4+}$, to be present at pH near 2. The +6 form of TPyP exists only at very high hydrogen ion concentrations, near pH 0.[7] It is interesting to point out that the electronic spectra of the compound dissolved in organic solvents (with no aggregation taking place) are essentially similar to the spectrum of TPyP in an aqueous HCl solution at pH 2.3. This implies that the TPyP exists as a free base in organic solvents but does not confirm the

protonation state of the pyridyls in nonaqueous environments. The optical spectrum of the TSPP:TPyP adduct shows the presence of medium intensity bands near 420 nm and two weak bands near 493nm and 702 nm of about equal intensity which are absent in the spectra of the monomers. *J*-bands usually seen in the visible spectrum of the TSPP aggregates occur in a similar location (490 and 707 nm), but the Soret band is very sharp and nearly four times as intense of the associated Q-band.[8,9,10] We believe that the 422 nm band (*H*-aggregate) and red shifted 493 (*J*-aggregate) bands depicted in Fig. S1 are those of TSPP:TPyP adduct and not the TSPP self-aggregate. That being said, the UV-vis solution data is not really appropriate to analyze the electronic properties of the TSPP:TPyP self-assembled structures. Because these nanostructures increase in size with time the solution absorption spectra become more difficult to interpret. In order to avoid these complications, it would be more desirable to use diffuse reflectance spectroscopy to investigate the optical properties of the TSPP:TPyP solid. Such experiments will be performed shortly.

We studied the relative stoichiometries involved in forming the TSPP:TPyP binary aggregates at pH 2 by measuring the UV-visible spectra of porphyrin mixtures containing different ratios of TSPP and TPyP as a function of time. Fig. S2 presents the

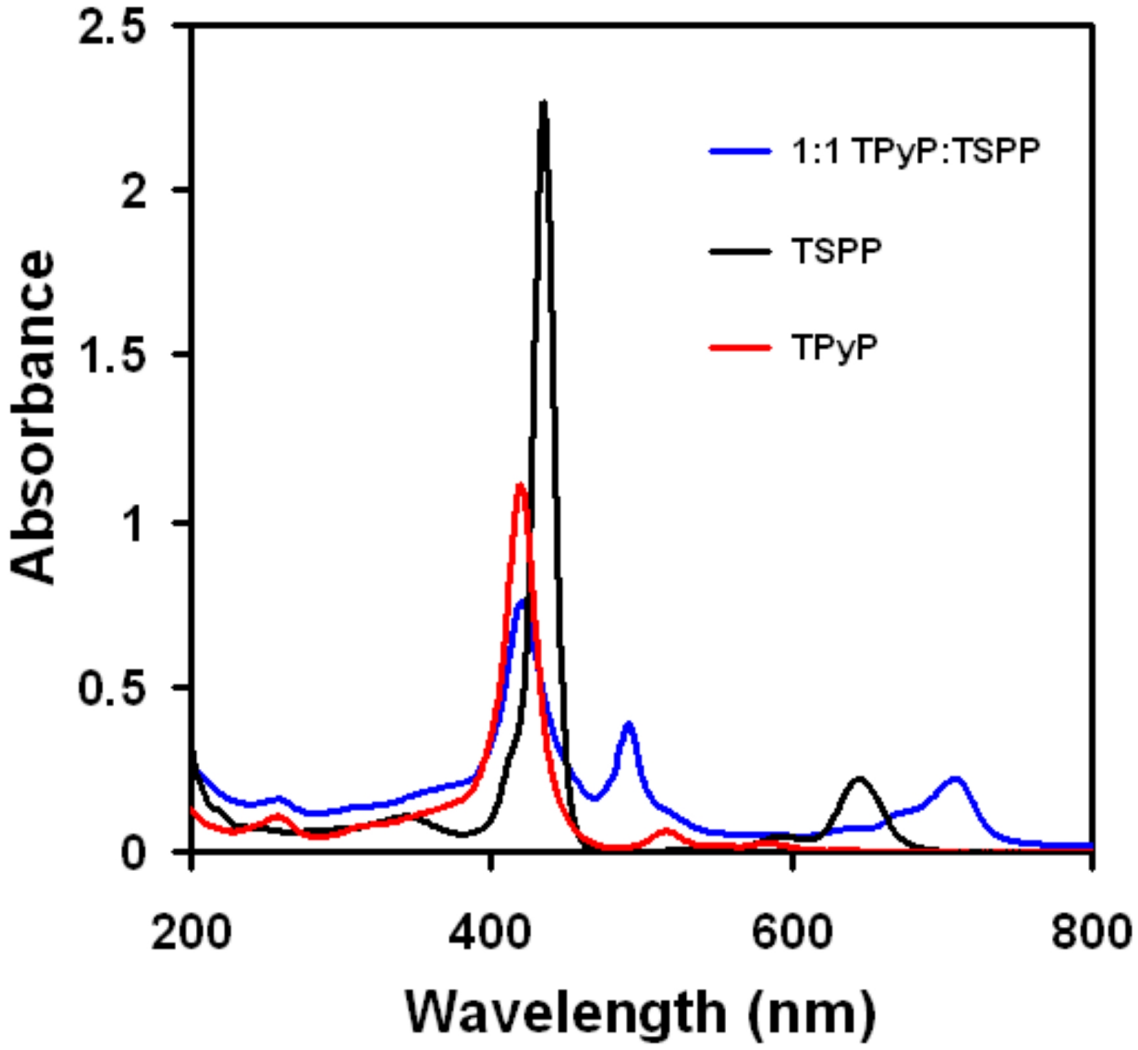

Fig. S1 UV-Visible spectra of 5 μM solutions of TSPP and TPyP at pH 2 and a 1:1 mixture of TSPP and TPyP at 5 μM (each) also at pH 2.

absorbance spectra of five different stoichiometric ratios of the parent ionic species adding up to a total concentration of 10 μM. The TSPP:TPyP mixtures were allowed to react for 5 weeks undisturbed during which time the nanostructures formed in solution and settled at the bottom of their respective vessels. After that time the solid TSPP:TPyP precipitates were isolated and the supernatants decanted and their optical spectra were measured (Fig. S2) By plotting the original stoichiometric ratios of TSPP:TPyP versus the difference in concentration of the same species remaining in the supernatant we found that the aggregation clearly favors a 1:1 ratio of the ionic tectons. In Fig. S3, we quantitatively summarize the spectral results depicted in Fig. S2. Here, the original TSPP:TPyP ratios employed are plotted against the concentration difference of TSPP and TPyP remaining in the supernatant. This porphyrin concentration difference was estimated by using the extinction coefficients associated with 434 nm and 420 nm Soret bands for TSPP and TPyP, respectively. Note that for the 1:1 ratio of TSPP to TPyP (denoted by the dashed line) the porphyrin concentration remaining in the supernatant is nearly zero, a sure indication of the nearly complete aggregation. We also observed that when excess of TPyP was present, a 1:1 CBI solid was still formed and the unreacted TPyP remained in solution. However, when the TSPP was in excess, the supernatant spectra appeared to be complex

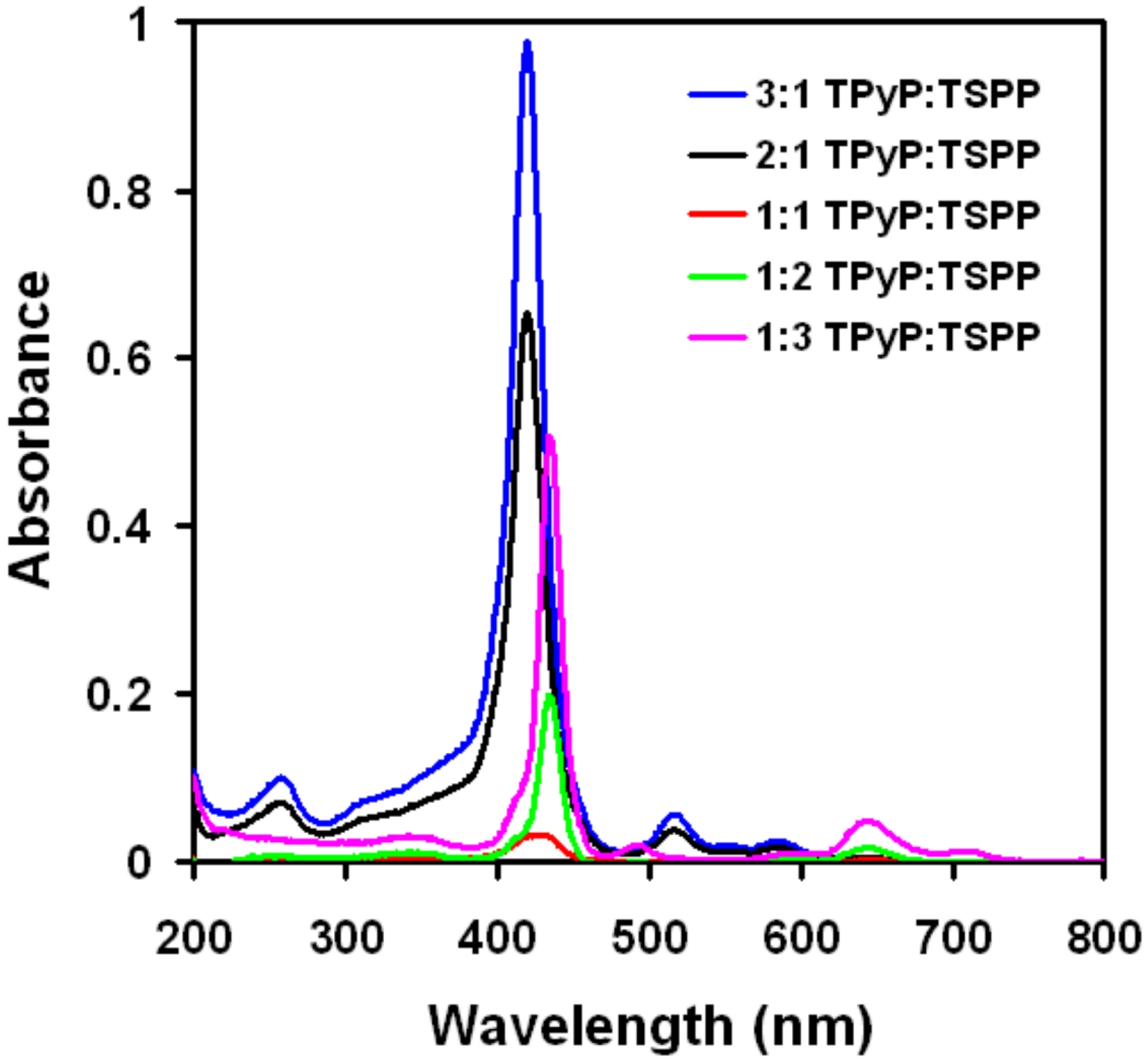

Fig. S2 UV-Visible spectra of 10 uM total porphyrin concentration solutions with varying ratios of TSPP and TPyP at pH 2. The mixtures were allowed to react undisturbed for five weeks in the absence of light.

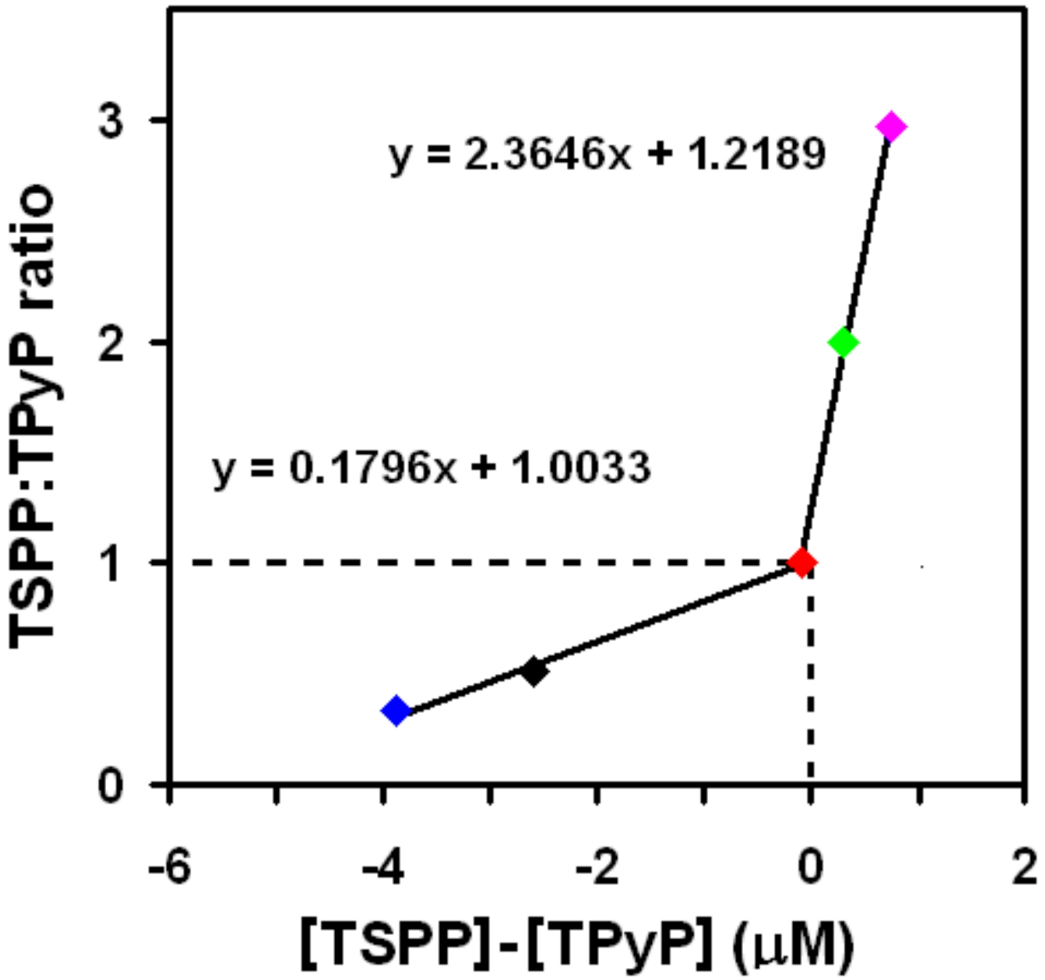

Fig. S3 Original stoichiometric ratios of TSPP to TPyP at 10 uM total porphyrin concentration in solutions versus the difference in concentration of the same species remaining in the supernatant after aggregation. The concentration difference of TSPP to TPyP in the supernatant was calculated by using the Soret band absorbencies and their extinction coefficients for TSPP and TPyP, repetitively. The dashed line is a guide for the 1:1 ratio TSPP:TPyP aggregation experiment results.

suggesting that possibly self-aggregated TSPP was present.

Our XPS results and the elemental analysis of the TSPP:TPyP solid composite reinforce the a 1:1 stoichiometric porphyrin ratio established by the UV-vis studies. We did observe variable amounts of residual chlorine in our solid samples but this element was easily removed by annealing the solid to above 100°C. The relative amounts of other elements and the morphological and crystallographic properties of the TSPP:TPyP solid were not altered by heating. Since no other ionic species were detected, the possible porphyrin ion pairs that make up the nanostructures are either $[H_4TSPP]^{2-}$: $H_2[H_2TPyP]^{2+}$ (with only two protonated pyridyl nitrogens) or $1[H_4TSPP]^{2-}$: 0.5 $H_4[H_2TPyP]^{4+}$: 0.5 H_2TPyP. Both tecton combinations preserve charge neutrality in the solid state. In a pH 2 solution it is less clear which ionic species combinations predominate.

Shelnutt and coworkers combined $[H_4TPPS]^{2-}$ and tin substituted TPyP, $H_4[SnTPyP]^{4+}$ at pH 2 in 0.01M HCl. They determined the ratio of the tectons was charge consistent with 2.0–2.5 H_4TSPP to 1.0 SnTPyP by EDX and optical spectroscopy. Clearly, incorporation of a metal into the ring of one of the tectons affects charge stabilization on the porphyrins, which in turn affects the stoichiometry of the ionic coupling.

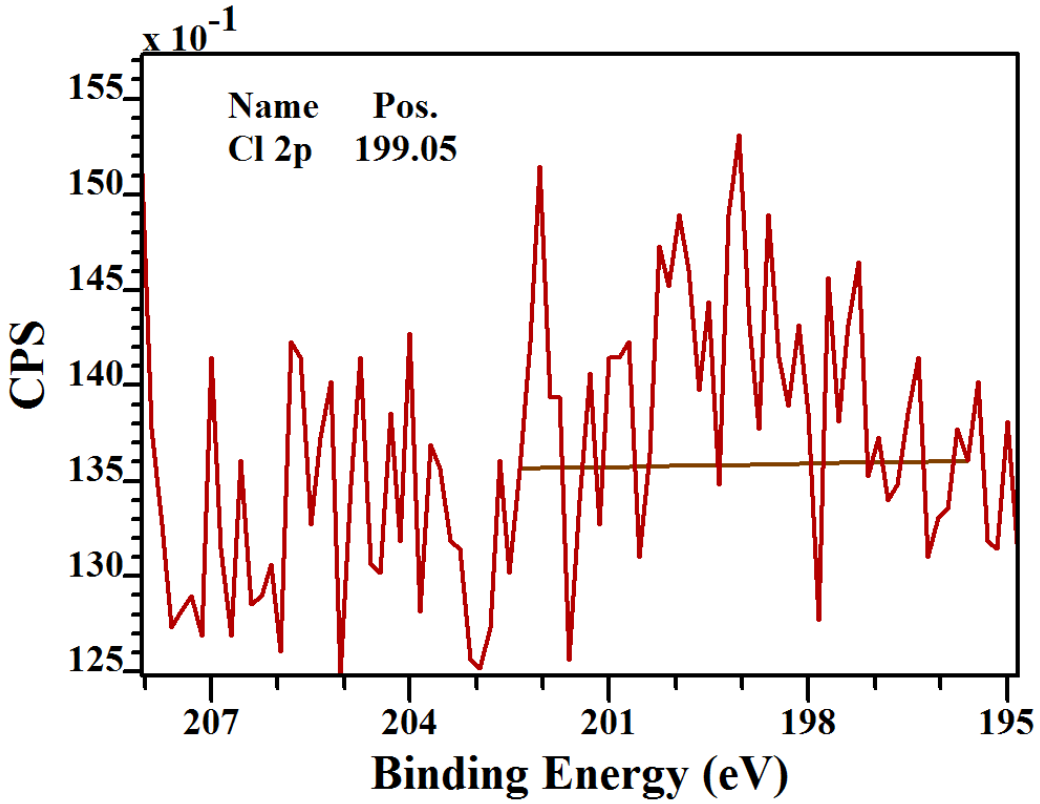

Fig. S4 Cl 2p XPS region for TSPP:TPyP nanorods measured after heating the sample for 30 min at 130°C.

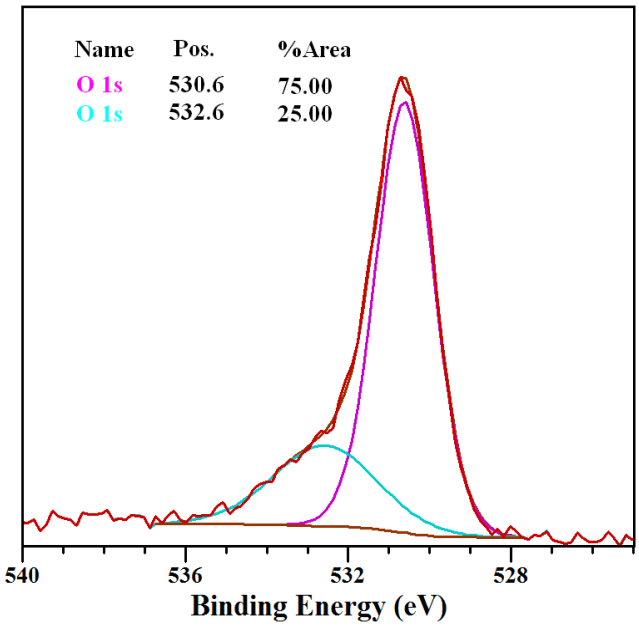

Fig. S5 O1s region XPS for TSPP:TPyP nanorod powder obtained after heating the sample at 150°C for 30 minutes. The colored line fits are associated with the binding energies arising from the oxygen bound to sulfur (pink) and oxygen in a hydroxyl group (blue). The relative areas under each curve are also given.

XPS chlorine and oxygen binding energies acquired from TSPP:TPyP rods before and after heating

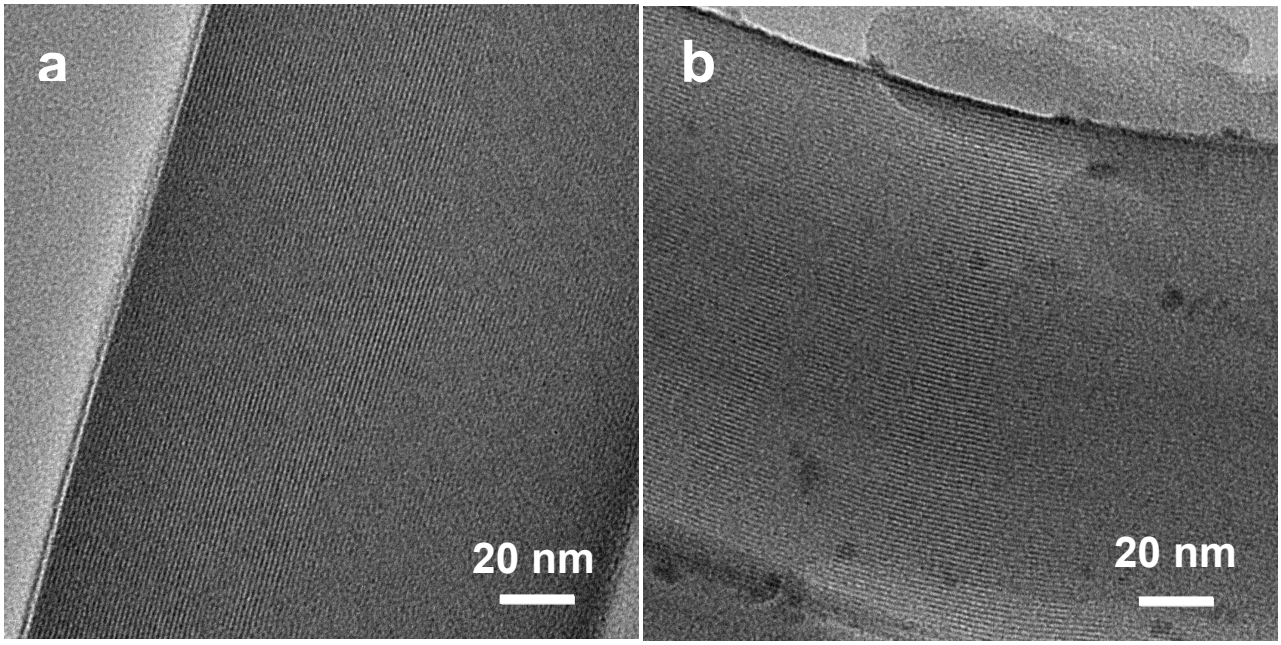

Fig. S6 HRTEM images of TSPP:TPyP nanorods on deposited on carbon coated Ni grids: (a) at room temperature and (b) after heating to 110°C for 30 minutes.

In the XPS spectrum of the unheated sample of the TSPP:TPyP nanorods. We observe a weak band above the noise at 198.eV that can be deconvoluted into $Cl2p_{3/2}$ and $Cl2p_{1/2}$ peaks. However, the chlorine signal disappears completely when the nanorods are heated to a temperature of 110 C or higher. In Fig. S4, the chlorine signal is barely detectable in the noise in the XPS spectrum of the TSPP:TPyP heated to 130°C.

The O1s region of the XPS spectrum of the unheated sample of the TSPP:TPyP solid displays a two band fit of the O 1s signal having binding energies near 530 and 532 eV in a 2:1 ratio, with the lower value assigned to the oxygen bound to sulfur. The higher binding energy at 522 eV is attributed to the oxygen of a water molecule. The oxygen to sulfur ratio from the XPS data for the unheated TSPP:TPyP sample is 4.5:1. We explain the 2:1 ratio of the two different oxygens in the sample as follows. The TSPP has four sulfonate groups each bearing 3 oxygens for a total of 12 oxygens per molecule. By multiplying 4 (the number of sulfurs present) times 4.5 we get a total of 18 oxygens. Thus, 12 out of 18 oxygens would give 66.6% or 2/3 of the oxygens bound to the sulfurs. The other six oxygens may be explained by water molecules in the crystalline structure and trapped HCl-H_2O. A small amount of trapped pH 2 solution would explain both the excess water and trace HCl. Elemental analysis results are in good agreement with the O:S ratio.

Fig. S5 presents the O1s region of the XPS spectrum of TSPP:TPyP solid after heating at 150°C for 30 minutes. The oxygen to sulfur ratio was measured to be to 4:1. Again, assigning 12 oxygens to 4 sulfurs yields 4 extra oxygens. This suggests that there may be 4 water molecules per TSPP:TPyP actually incorporated in the crystal structure.

HRTEM images of the TSPP:TPyP rods before and after heating

Fig. S6 provides high resolution TEM images of TSPP:TPyP nanorods before and after heating the sample to 110 C for 30 min. Both Fig. S6a and S6b, show clear fringes indicating that the rods are crystalline and experience no amorphization after heating.

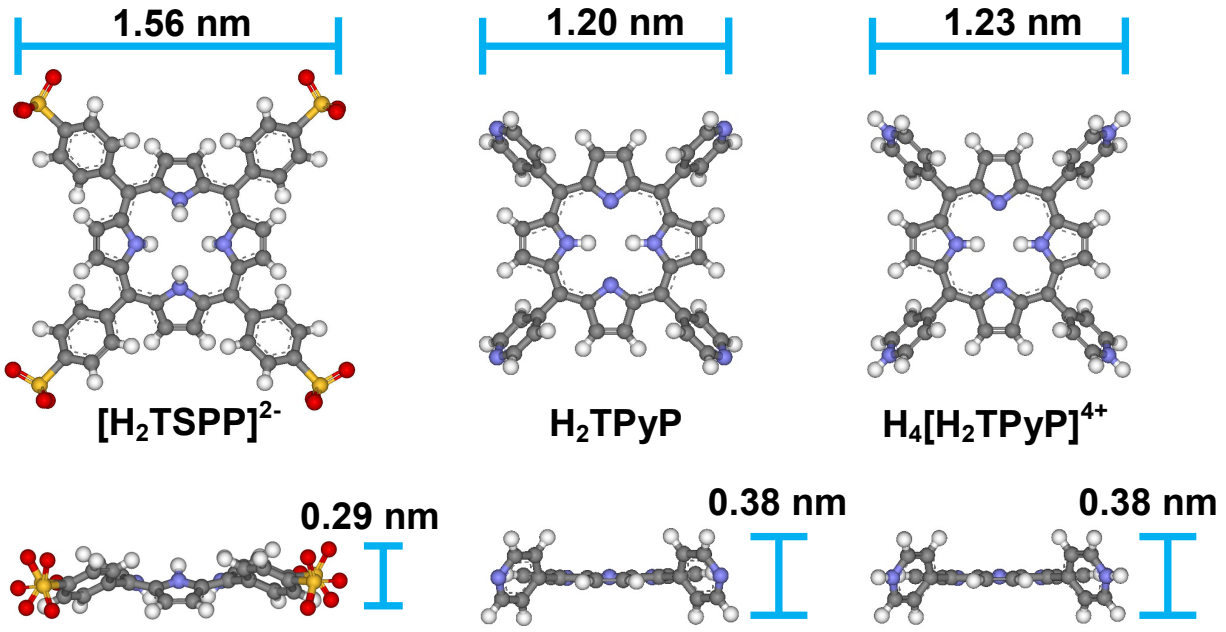

Fig. S7 Top and side views of geometry optimized structures of the $[H_2TSPP]^{2-}$, $H_2[H_2TPyP]^{2+}$, and $H_4[H_2TPyP]$ tectons. These structures are based on DFT calculations using the B3LYP functional and the 6-31þG(d,p) and the 6-311++G basis. The bars are distances between the indicated atoms.

The spacing between the lines is about 1.5 nm, which is consistent with the distance between the centers of two porphyrins, positioned side by side with their cores in perpendicular orientation relative to the substrate.

Calculations and Modeling

Structural calculations and geometry optimizations of the ionized species were performed using the commercial program Gaussian 03. The results are depicted in Fig. S7.

Determination of Young's modulus of the TSPP:TPyP nanorods

Young's modulus measurements were made using a Bruker Multimode 8 AFM with Nanoscope V controller and J "vertical" scanner and a lateral force Digital Instruments AFM. Bruker's Nanoscope 8.15 software was used in the acquisition of data. Cantilevers employed were antimony doped silicon with lengths of 110 and 120 um, resonance frequency of 130 – 140 kHz, and spring constant 2 - 4 N/m. In agreement with the literature,[11,12] the best force-curve results were observed with a dulled tip. Sharp probes may have nanoasperities at the very end of the tip that impact the contact area and adhesion forces.[13, 14] Accordingly, all new probe tips were mechanically polished by scanning on a commercially available sapphire standard (Bruker) prior to indentation experiments. Each tip was characterized by performing a 2 um (512 lines) scan on a commercially available titanium roughness standard (Bruker) with the Bruker's ScanAsyst® to enable optimum characterization of the dulled tip without further dulling. Tip shape was deconvoluted from the sharp points of the deposited titanium nanoplates using Bruker's Nanoscope Analysis software. The deconvoluted tip shape was used for the determination of the tip radius in the effective Young's modulus curve fitting of the force curves.

The spring constant of the AFM cantilever was determined using the Sader method.[15] A thermal tune was acquired in air and fit using a damped harmonic oscillator model to determine the resonance frequency (ω_{air}) and Q-factor (Q_{air}) in air. Microscope

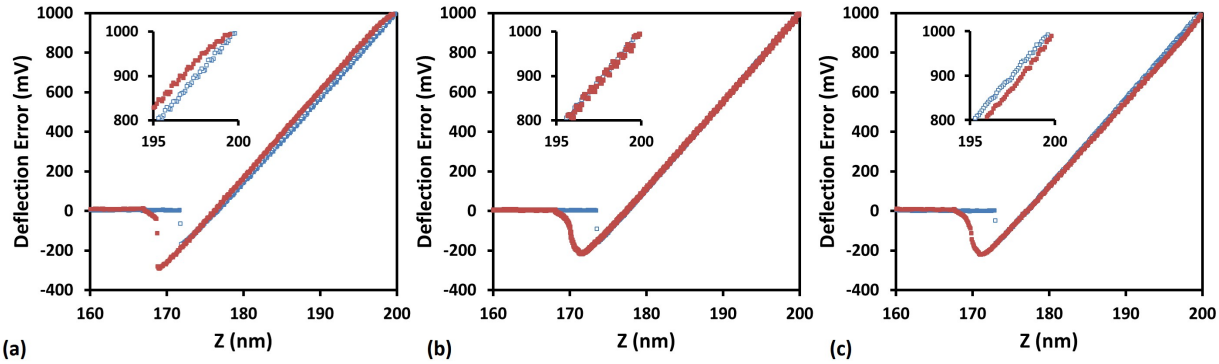

Fig. S8 Comparison of the effects of the x-rotate setting on the deflection-Z curve shape showing the impact on the retract curve in the top 10 percent of the maximum load. Ramps were performed at 1Hz ramp rate, 200 nm ramp size, 1000 mV trigger threshold, and 2048 points per line are shown. (a) 0 degrees, (b) 32 degrees, (c) 50 degrees.

images in top-down view were used to evaluate the length (L) and width (b) of the cantilevers used. The microscope camera was calibrated by taking an image of a 10 µm pitch AFM calibration standard (Bruker). Image J software was used to extract values of L and b from the calibration grid and cantilever images. The density of air (ρ_{air}) was determined by using the ideal gas law. The density of air did not change dramatically and was calculated to be 1.097 kg m^3. The viscosity of air (η_{air}) was assumed to be 1.86x10^{-5} kg m^{-1} s^{-1}. The resonance frequency (ω_{air}), Q_{air}, L, b, ρ_{air}, and η_{air} were used to solve for the spring constant of the cantilever using an online solver developed by John Sader (http://www.ampc.ms.unimelb.edu.au/afm/calibration.html). This solver uses the following equation:

$$k = 0.1906\rho_{air}b^2LQ_{air}\Gamma_i(\omega_{air})\omega_{air}^2$$

where $\Gamma_i(\omega_{air})$ is the imaginary part of the hydrodynamic function and is dependent on the Reynolds number (Re) where $Re = \rho_{air}\omega_{air}b^2/(4\eta_{air})$. The spring constants of the two cantilevers used were determined to be 2.91 N m^{-1} and 3.65 N m^{-1}.

In order to determine the deflection sensitivity of the AFM cantilever, single ramps were taken on both Sapphire and Mica. Both of these samples are good candidates for the cantilevers used as they are hard materials with Young's modulus values of 441 GPa [16] and 137 GPa [17] respectively. The following collection parameters were used: 200 nm ramp size, 1 Hz ramp rate, 2048 number of samples, 32 degree x-rotate, and a series of 5 ramps each at a relative trigger threshold of 300, 400, 500, 750, 1000, 1250, 1500, 1750, and 2000 mV. The 32 degree x-rotate was determined by inspection of the approach and retract force-curves on sapphire at higher relative trigger thresholds (1000, 1500, and 2000 mV).

The x-rotate setting is normally used to prevent plowing of the sample as the tip interacts with the sample and the cantilever bends.[18,19] Prior to the tip touching the surface, the cantilever is oriented at an angle relative to the surface, approximately 10 degrees. As the cantilever bends the tip indents the surface and at large enough deflection, the bending of the cantilever causes a lateral displacement of the tip. This displacement can occur in the x direction (aligned along the cantilever) and even in the y direction due to torsion of the cantilever. To help compensate for this displacement of the tip the piezo is moved in the x direction of the displacement. In our work, it was noticed that at zero degree x-rotate the top portion of the retract curve was not in line with the top portion of the approach curve. Generally the top ~10 percent of the maximum load of the curve had a slope smaller than the approach curve causing the retract curve to trail behind the approach curve. After the top 10 percent, the slope of the retract curve increased. This increase in slope generally caused the retract curve to cross back over the approach curve down to the adhesion region. This may be due to lateral friction forces caused by the tip being dragged along the surface back toward the initial starting point as the cantilever relaxes and the sample is retracted. By increasing the x-rotate the discrepancy between the curves decreased until they were in line with one another at a value of 32 degrees. By going beyond the 32 degree x-

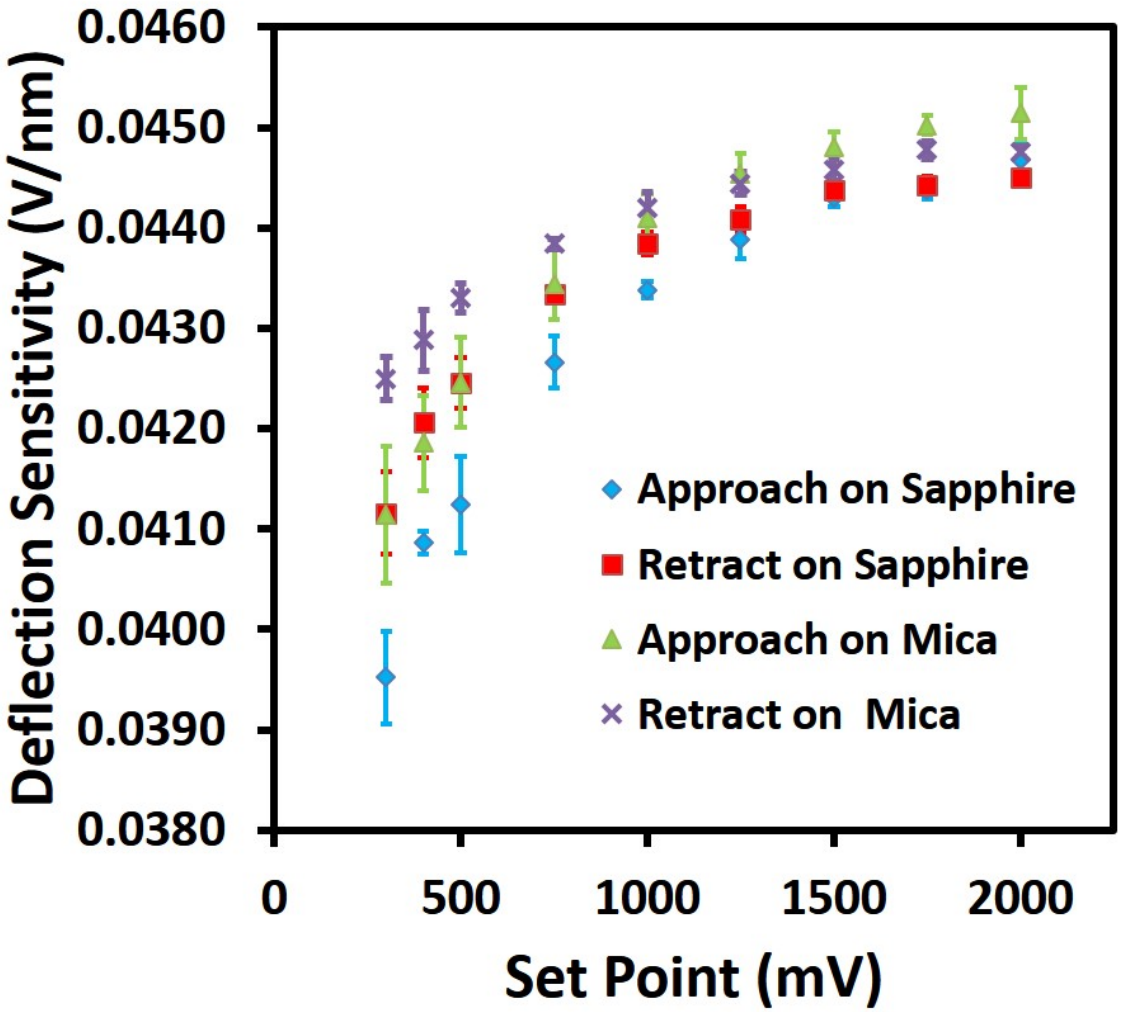

Fig. S9 Graph of deflection sensitivity obtained from a linear fit of the contact region of both the approach and retract curves from force curves obtained on sapphire and mica with the 3.65 N/m spring constant cantilever.

rotate to 50 degrees, the top 10 percent of the maximum load of the retract curve had a greater slope causing it to bend below the approach curve. After the top 10 percent the slope of the retract curve decreased causing a bend in the curve. This may be due to a release in tension as the sample is moved in the x-direction causing a sudden drop in force. Thus, a 32 degree x-rotate was chosen. These results are consistent with those observed in the literature. All of these changes may be seen in Fig. S8.

A 1 Hz ramp rate was chosen to minimize hysteresis due to the scanner creep. Scanner creep causes the retract curve to have a slope less than that of the approach curve in the contact region. At slower scan rates, 0.25 Hz, the signal to noise is better; however, this difference between approach and retract curves is more pronounced.

The slopes of the approach and retract curves on sapphire and mica were taken to determine the deflection sensitivity of the cantilever using Bruker's Nanoscope Analysis software. A linear least squares fit region was selected between about 95% of the max load and zero deflection error on the contact region of the retract curve. The average of 5 ramps was used to determine the deflection sensitivity at each trigger threshold. The deflection sensitivity was plotted as a function of the deflection error set point voltage. At the higher forces, the difference between the deflection sensitivity of the approach and retract curve becomes negligible. We have chosen to use only the retract curves for the determination of the deflection sensitivity and fitting for the

Young's modulus on our samples, because the sample may plastically deform, especially on softer samples, while loading. This plastic deformation would cause a significant change in shape of the contact region of the approach curve, making it a more complex problem.

Looking at Fig. S9, it appears that the deflection sensitivity approaches a maximum at higher deflection error set points. The large error at lower set points may be attributed to fitting fewer data points in the contact region in comparison to the higher set points. The asymptotic behavior is reasonable due to the force curves not being a perfectly straight line in the contact region as noted by Oliver and Pharr and as seen in the DMT model fits of the data shown later. Thus, at the higher forces (set point voltages), the apparent deflection sensitivity would not be expected to change as much as at the lower forces near the adhesion region. Near the adhesion region the slope of the force curve becomes less linear. This may be partially attributable to the nature of the adhesive interactions and may vary by sample. By using the deflection sensitivity obtained from fitting the higher forces, we are able to isolate the movement of the cantilever relative to the movement of the piezo from the complex adhesive interactions near the jump-to-contact and pull-off regions. Thus we should obtain more consistent results on a known standard or sample of unknown adhesive and elastic properties. This is true for our measurements. We chose to use the deflection sensitivity at 2000 mV. Looking at a HOPG standard we were able to obtain consistent results consistent with the literature values over the range of set points (300 – 2000 mV) used in our experiments on HOPG. From these results we conclude that the maximum deflection sensitivity may be attributed to the intrinsic response of the cantilever. We used the same deflection sensitivity when analyzing our nanorod samples, however, we limited the maximum set point to 1000 mV. This choice was made due to plastic deformations and tip changes at higher set points.

We then checked the calibration of our cantilever and tip by examining a freshly peeled HOPG sample and fitting the curves with the DMT model using Mathcad® software. The HOPG was peeled using adhesive tape to give a clean flat surface. The same ramp conditions as the calibration on sapphire and mica were used over the same trigger threshold ranges. The nominal Young's modulus of HOPG according to Bruker is 18 GPa.[20] Other literature sources report 15-30 GPa. [21,23]

Force versus separation curves were obtained by using the maximum deflection sensitivity at 2000 mV deflection and the calculated spring constant were input into the software. We calculated and plotted the force vs. separation curves from the deflection error voltage vs. distance curves using the following equations in Mathcad 14®. First the deflection of the cantilever in nm at each point was obtained by using:

$$d = V / D$$

where d is the deflection in nm, V is the deflection error in (V), and D is the calibrated deflection sensitivity in V/nm. D is taken to be a constant. Next, to calculate the indentation the equation

$$i = (z - d) - h$$

was used, i is the indentation in nm, z is the z-piezo position in nm, d is the deflection in nm, and h is a constant used to set the zero indentation at the point of maximum adhesion force (F_{adh}).

The force at each point is then calculated using the calculated spring constant of the cantilever and the Hooke's Law equation:

$$F = k (d)$$

where F is the force in nN, k is the spring constant in nN/nm , and d is the deflection in nm.

Force versus separation retract curves obtained on HOPG were least squares fit using the Derjaguin, Muller, and Toporov (DMT)[24] model in Mathcad® software to determine the Young's modulus E. The following equations are utilized:

$$F_{Tip} = 4/3\ E^* (R_{Tip})^{1/2} (i)^{3/2} + F_{adh}$$

where F_{Tip} is the force measured at each point in nN, E^* is the reduced Young's modulus in GPa, R_{Tip} is the tip radius in nm, F_{adh} is the force of adhesion or the pull-off force, and i is the indentation in nm. The initial point of zero indentation, i_0, is set to the point at maximum adhesion, F_{adh}. The actual point of zero indentation is determined by a least squares fit of the data. The maximum indentation i_{max} is set to the point of maximum applied tip force or force setpoint.

The reduced Young's modulus is related to the Young's modulus and Poisson's ratio of the tip and sample by the following equation:

$$1/E^* = (1 - v_{tip}^2) / E_{Tip} + (1 - v_s^2) / E_s$$

where v_{tip} and E_{Tip} are the Poisson's ratio and Young's modulus of the AFM tip material and v_s and E_s are the Poisson's ratio and Young's modulus of the sample.

An E^* and s_m of 20 GPa and 1 nm respectively were used as our initial guesses and an R_{Tip} of 1 nm was used for the least squares fit. We determined the tip radius as a function of indentation depth from 0 to 4 nm in 0.05 nm increments using the Nanoscope Analysis software and the deconvoluted tip from the scanned image of the titanium roughness sample obtained by a blind reconstruction type of method.[25,26] R_{Tip} is effectively the radius of a sphere fit to the range defined by the cross-section of the deconvoluted tip at a specified height from the apex of the tip. We then fit the tip radius and indentation depth with a 12th order polynomial fit in Mathcad. The tip radius (R_{Tip}) was then extrapolated from this fit using the indentation depth for each ramp. The E^* was corrected by dividing by $(R_{Tip})^{1/2}$. We then obtained the Young's modulus from the reduced Young's modulus using

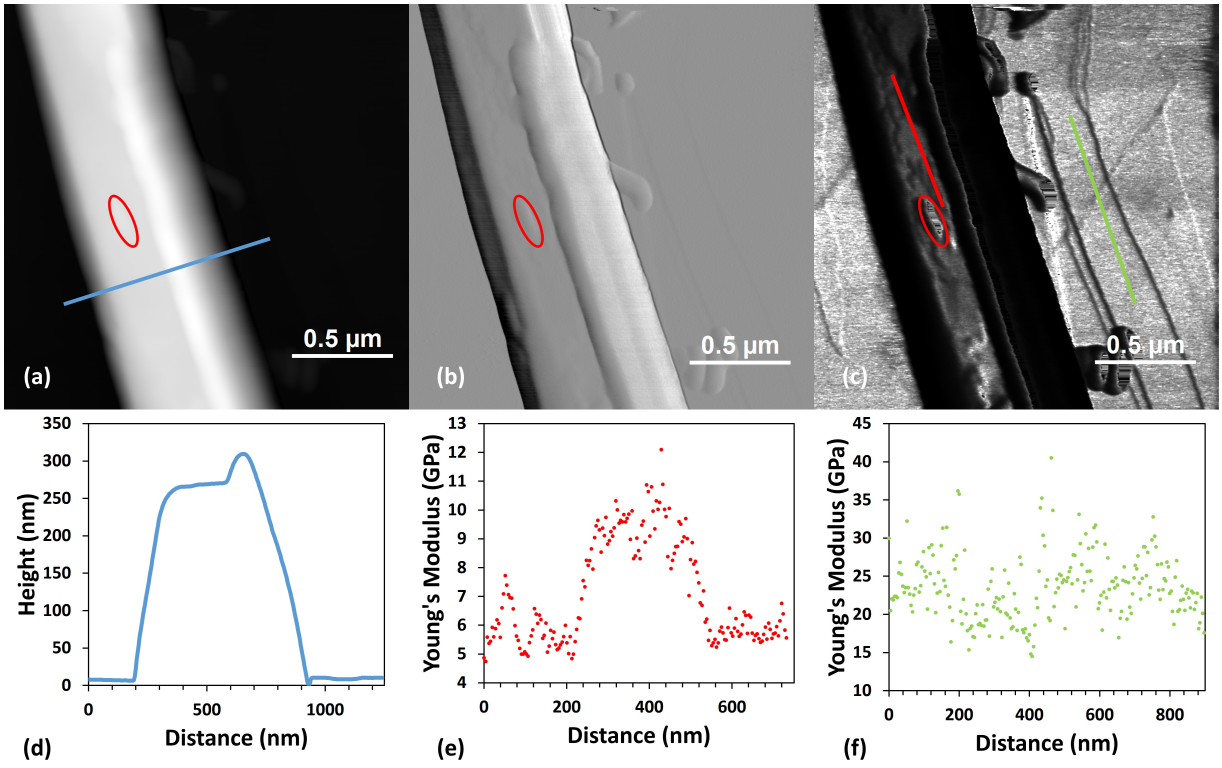

Fig. S10 AFM micrograph of a 250 nm TSPP:TPyP nanorod. (a) Height plot, (b) Deflection error plot, (c) PF-QNM plot of the Young's modulus, (d) Height vs distance plot across the nanorod, (e) Young's modulus along the length of the nanorod, (f) Young's Modulus of the HOPG substrate.

v_s = 0.24 for HOPG and 0.3 for the nanorods, v_{tip} = 0.22, and E_{Tip} = 166 GPa for the silicon cantilever.

In addition to single ramps, we also performed PeakForce Quantitative Nannomechanical measurements (PF-QNM). We attempted to mimic the same parameters as those used for the single ramps. The parameters used are a 2 µm scan size, a setpoint of 500 mV, 1 Hz scan rate, with 512 points per line, and a PeakForce drive amplitude of 100 nm resulting in 200 nm ramps. We used SPIP software to analyze the AFM micrographs.[27] A typical PF-QNM image of a 250 nm TSPP:TPyP nanorod is shown in Fig. S10. This image was taken using the 3.65 N/m cantilever. From the single ramps we determined an average tip radius of about 25 nm for a 500 mV (41 nN) setpoint. From the cross-sections of the DMT Young's modulus image we observe similar Young's modulus values to those obtained from the single ramps on both the nanorod and on HOPG. We did observe plowing of the nanorod on the right side due to the bending of the cantilever with no option for an x-rotate adjustment as was possible for the single ramps. Only the Young's modulus values on the top of the nanorod away from the plowed side of the nanorod were used in determining the Young's modulus of the nanorod.

The decrease in the Young's modulus values on the sides of the rod may be attributable to a change in the tip radius caused by the side of the AFM tip coming in contact with the nanorod. Additionally a defect can be seen in the nanorod as evidenced by a dramatic increase in the Young's modulus beyond the range detectable by the cantilever shown by the red oval in Fig. S10.

References

1 A.D. Schwab, D.E. Smith, C.S. Rich, E.R. Young, W.F. Smith, and J.C. de Paula, *J. Phys. Chem. B,* 2003, **107**, 11339-11345.

2 M.M. Kruk and S.E. Braslavsky, *J. Phys. Chem. A,* 2006, **110**, 3414-3425.

3 A. Farjtabar and F. Gharib, *J. Solution Chem.,* 2010, **39**, 231–244.

4 S.M. Vlaming, R. Augulls, M.C.A. Stuart, J. Knoester, and P.H.M. Loosdrecht, *J. Phys. Chem. B,* 2009, **113**, 2273-2283.

5 E.B. Fleischer and L.E. Webb, *Inorg. Chem.,* 1963, **67**, 1131-1133.

6 Z. Wang, C.J. Medforth, and J.A. Shelnutt, *J. Am. Chem. Soc.,* 2004, **126**, 15954-15955.

7 S. Zakavi, A.G. Mojarrad, and T.M. Yazdely, *Macroheterocycles,* 2012*,* **5,** 67-71.

8 C.J. Medforth and J.A. Shelnutt, in *Handbook of Porphyrin Science*, ed. K. M. Kadish, K. M. Smith, and R. Guilard, World Scientific Publishing, 2011, **11**,181-222.

9 S. Liu, W. M. Wang, A. L. Briseno, S. C. B. Mannsfeld, and Z. Bao, *Adv. Mater.,* 2009*,* **21**, 1217-1232.

10 V. C. Sundar, J. Zaumseil, V. Podzorov, E. Menard, R.L. Willett, T. Someya, M. E. Gershenson, and J. A. Rogers, *Science,* 2004, **303**, 1644-1646.

11 M.E. Dokukin and I. Sokolov, *Macromolecules,* 2012, **45**, 4277-4288.

12 M.E. Dokukin and I. Sokolov, *Langmuir,* 2012, **28**, 16060-16071.

13 S. R. Cohen, *Ultramicroscopy,* 1992, **42-44**, 66-72.

14 S.R. Cohen, G. Neubauer, and G. M. McClelland, *J. Vac. Sci. Technol. A,* 1990, **8**, 3449-3454.

15 J.E. Sader, J. W. M. Chon, and P. Mulvaney, *Rev. Sci. Instrum.,* 1999, **70**, 3967-3969.

16 W.C. Oliver and G. M. Pharr, *J. Mater. Res.,* 1992, **7,** 1546-1583.

17 T. Oshiro, A. Backstrom, A.-M. Cumberlidge, K. W. Hipps, and U. Mazur, S. P. Pevovar, D. F. Bahr, and J. Smieja, *J. Mater. Res.,* 2004, **19**, 1461-1470.

18 B. Cappella and G. Dietler, *Surf. Sci. Rep.,* 1999, **34**, 1-104.

19 M. VanLandingham, *Microscopy Today*, 1997, **10**, 12-15.

20 *PF-QNM User Guide Rev F.*, Bruker Corporation, 2009, p.51.

21 T. Tsuji and K. Yamanaka, *Nanotechnology,* 2001, **12**, 301-307.

22 D.M. Schaefer, A. Patil, R.P. Andres, and R. Reifenberger, in *Atomic Force Microscopy/scanning Tunneling Microscopy*, ed. S.H. Cohen, Mona T. Bray, and M. L. Lightbody, Plenum Press, 1994, pp. 411-421.

23 K. Yamanaka, T. Tsuji, A. Noguchi, T. Koike, and T. Mihara, *Rev. Sci. Instrum.,* 2000, **71**, 2403-2408.

24 B.V. Derjaguin, V. M. Muller, and Y.U. P. Toporov, *J. Colloid Interface Sci.,* 1975, **53**, 314-326.

25 J.S. Villarubia, *J. Res. Nat. Inst. Stand. Technol.,* 1997, **102**, 435-454.

26 P.M. Williams, K.M. Shakesheff, M.C. Davies, D.E. Jackson, C.J. Roberts, *J. Vac. Sci. Tech. B,* 1996, **14**, 1557-1562.

27 SPIP software, Version 6.0.2. Published by Image Metrology A/S, Hørsholm, Denmark.